

Effects of rescanning parameters on densification and microstructural refinement of 316L stainless steel fabricated by laser powder bed fusion

Anqi Liang^A, Khee Siang Pey^A, Tomas Polcar^A, Andrew R. Hamilton^{A*}

^A Engineering and Physical Sciences, University of Southampton, Southampton, SO17 1BJ, United Kingdom

Corresponding author: Andrew R. Hamilton. Email address: a.r.hamilton@soton.ac.uk.

Abstract:

A challenge with microstructural control and refinement in laser powder bed fusion (LPBF) is maintaining high density when choosing parameters for desired microstructures. Rescanning during LPBF has been reported to improve densification and decrease surface roughness for many different alloys. However, little has been reported regarding the effects of locally rescanning with varying processing parameters on sub-grain cell size refinement for 316L stainless steel (SS). This study presents a novel solution to enable high densification with microstructural control in 316L SS by using a set of initial scanning parameters to achieve densification and a different set of rescanning parameters to refine the microstructure. Results showed that rescanning resulted in heterogeneous microstructure with coarse cell size of 0.84 μm and locally refined cell size of 0.35 μm , while maintaining a high level of densification (99.96%), therefore enabling potential variations in component strength and hardness. The spatial distribution of local microstructure refinement was dictated by the melt pool dimensions of initial scanning and rescanning relative to the powder layer thickness. To better understand the link between LPBF process parameters and microstructure, the Wilson-Rosenthal equation was used to predict cooling rate ($G \times R$) and correlate with sub-grain cell size. Such variation in properties may be useful for applications requiring parts with hardened surfaces, or localized strengthening at stress concentrations and sites of expected failure.

Keywords: laser powder bed fusion, Wilson-Rosenthal equation, 316L stainless steel, heterogeneous microstructure, sub-grain cell size, density.

1. Introduction

The high temperature gradients and rapid solidification rates observed in laser powder bed fusion (LPBF) additive manufacturing (AM) lead to non-equilibrium microstructures with potentially significant effects on the properties of the resulting material. In the case of 316L austenitic stainless steel (SS), LPBF processing conditions lead to the formation of cellular/dendritic sub-grain structures, associated with compositional segregation, the size of which is reported to correlate with strength according to a Hall-Petch type relationship (Wang et al., 2018). This relationship describes a trend of increasing strength and hardness with decreasing sub-grain cell size and has been attributed to high dislocation densities at cell walls that prevent dislocation motion along continuous slip planes. Simulations suggest that oxide precipitates within cell walls may also play a role in this strengthening effect (Collins et al., 2016).

The sub-grain cell size has been reported to vary with changes in the laser power (P) and scanning speed (v) used in LPBF. Changes in these parameters can affect the temperature gradient at the solid-liquid interface (G) during solidification of the melt pool, and the growth rate of the solidifying front (R). The cooling rate of material during solidification is represented by the product $G \times R$, which determines the size-scale of the resulting microstructure, with finer microstructures achieved at higher cooling rates. Scipioni Bertoli et al. (2019) reported that the Wilson-Rosenthal equation, an analytical model for temperature fields around a point heat source, predicted an inverse relation between the ratio P/v and cooling rate ($G \times R$), and that increasing $G \times R$ correlated with smaller cell size and higher yield strength (from 441 to 517 MPa) in 316L SS. Wider

ranges of yield strength from 325 MPa to 700 MPa have been predicted by simulations of increased scan speed and decreased laser power due to the finer predicted microstructure and faster predicted cooling rates (Clymer et al., 2017). An increase of yield strength in LPBF 316L SS from 339.2 MPa to 519.8 MPa was reported by Wang et al. (2018) upon refinement of primary dendrite arm spacing (*PDAS*) from 0.81 μm to 0.37 μm due to changes in part geometry and thus suspected cooling rate. Li et al. (2020) have reported that it is dislocation density around these cells, rather than segregation cell size, that accounts for strengthening and so better correlates with yield strength changes. Alongside increased strength with decreased cell size, Scipioni Bertoli et al. (2019) also reported differences in porosity and corresponding decreases in ductility (from >40% to 21%), highlighting the challenge that changing process parameters to change cell size and strength can also affect densification and porosity with detrimental mechanical effects. In related work from Niendorf et al. (2014), the microstructure and properties of 316L SS were varied by varying process parameters within a build to create graded heterogeneous materials. Laser powers of 400 W (fine-grained region) and 1000 W (coarse-grained region) were employed using a specialised LPBF system with two lasers, and a corresponding decrease in yield strength from 520 MPa to 400 MPa was observed.

Correlations between porosity and LPBF processing parameters are commonly made using energy density (E), which is a measure of the amount of energy per unit volume radiated to the powder bed at the focal point of the laser (Zhang et al., 2017). It can be calculated from P , v , the powder layer thickness t , and the hatch spacing h between laser scans:

$$E = \frac{P}{v \times h \times t} \quad (1)$$

At low energy densities increasing E can decrease porosity, but at higher energy densities further increases tend to increase porosity. Cherry et al. (2014) reported that increasing E from 41.81 J/mm³ to 104.52 J/mm³ increased density of 316L SS part from 91.16% to 99.62%, and increased hardness from 162 HV to a maximum of 225 HV. However, with further increases in E up to 209.03 J/mm³, hardness dropped due to decreases in density. Porosity in excess of 5% has been reported to significantly decrease tensile strength from a maximum of 590 MPa at 97.5% relative density to 530 MPa below 95%. It has also been reported that low levels of porosity <1% do not significantly influence micro-hardness due to the high ductility of 316L SS (Yusuf et al., 2017).

Another strategy to influence microstructural features and material properties during LPBF is to implement laser rescanning, in which the laser scans the same position multiple times. Recent literature has reported rescanning of different alloys, such as Ti6Al4V (Xiao et al., 2020), SCM440 steel (Shiomi et al., 2004), 18Ni300 maraging steel (Demir and Previtali, 2017), 316L SS (Yasa and Kruth, 2011), AlSi10Mg (Yu et al., 2019), Hastelloy X superalloys (Keller et al., 2020), Al-Mg-Zr (Griffiths et al., 2018), and Ti5Al2.5Sn (Wei et al., 2019). Most of these studies investigated the influence of rescanning on density and surface roughness only. For example, applying rescanning in LPBF of 316L SS showed that layer-by-layer rescanning with a higher energy density than initial scanning significantly increased density to almost 100% and decreased average surface roughness (R_a) by 87.5% (Yasa and Kruth, 2011). Improved densification (from 99.23% to 99.97%) was also reported for 18Ni300 maraging steel (Demir and Previtali, 2017). A few of studies have reported that rescanning with the same parameters as initial scanning resulted in grains with

different crystallographic orientation in Ti6Al4V (Tian et al., 2018) and shallower melt pools with finer grains in Al-Mg-Zr (Griffiths et al., 2018). A study on the microstructure and mechanical properties of Hastelloy X superalloys after rescanning with different laser powers found that the thermal gradient and cooling rates were modified, leading to finer dendrites, a change in strain hardening rate, and an increase in ductility (Keller et al., 2020). The effect of varying numbers of rescanning cycles (from 0–4) on mechanical properties was studied by Xiao et al. (2020), who reported that with increasing cycles, the ultimate tensile strength, yield strength, and micro-hardness all increased and reached a maximum after three cycles.

A challenge with microstructural control and refinement in LPBF is to maintain high density when choosing parameters for desired microstructures. A novel solution is to use a set of initial scanning parameters to achieve densification, and a different set of rescanning parameters to refine the microstructure. Rescanning is known as an effective strategy to improve density, however, the effects of rescanning with different parameters on local microstructure control for 316L SS have not yet been reported. The aim of this study was to implement localised rescanning of 316L SS using different rescanning parameters, and to explore the combined effects on both relative density and microstructural refinement. To help guide the design of localised microstructural changes, results were correlated with Wilson-Rosenthal equation predictions of cooling rate ($G \times R$) and melt pool dimensions. Results were also compared with single scan track experiments intended to rapidly screen for scanning and rescanning parameters that yield desired results.

2. Experimental procedure

2.1 Laser melting experiments and sample characterization

Gas-atomised 316L stainless steel powder (particle size normally distributed between 15 μm to 45 μm) used in this study was supplied by Carpenter (USA) as CT PowderRange 316L. The powder used in this study was a mixture of 10% fresh powder and 90% powder that was recovered from prior processing and sieved before reuse. The chemical composition specified by the manufacturer is listed in Table 1. Specimens were processed using a Concept Laser M2 LPBF 3D printer with a maximum laser power of 200 W operating in an inert argon gas environment.

Table 1 Chemical composition (wt. %) of 316L SS powders. (ADDITIVE, 2019a)

C	Fe	Cr	Ni	Mo	Mn	Si	N	O	P	S
< 0.03	Bal.	16 – 18	10 –14	2 – 3	< 2	< 1	0.1	0.1	< 0.045	< 0.03

The processing parameters in Table 2 were selected for single laser scan processing and scan tracks with a length of 10 mm were processed on a sand-blasted 316L stainless steel plate. Two tracks were scanned for each parameter. The distance between adjacent laser scans was 4 mm. A powder layer thickness of 30 μm was used in all cases.

Table 2 Parameters for single laser scan processing.

Laser power(W)	Scanning speed(mm/s)	Linear energy density (J/mm)	Laser power(W)	Scanning speed(mm/s)	Linear energy density (J/mm)
50	50	1.00	150	150	1
	200	0.25		600	0.25
	400	0.13		800	0.19
	600	0.08		1200	0.13
	800	0.06		1600	0.09
	1600	0.03		1800	0.08
	2400	0.02		2400	0.06
	3200	0.02		3200	0.05
100	100	1	200	50	4
	400	0.25		200	1
	800	0.13		800	0.25

1200	0.08	1600	0.13
1600	0.06	2400	0.08
2400	0.04	3200	0.06
3200	0.03		

After analysing the morphology and dimensions of single laser scan melt pools and the sub-grain cell size within the melt pool, several sets of parameters were selected to manufacture uniform cubes with size of 10 x 10 x 10 mm using 5 x 5 mm island scanning strategy to investigate the microstructure and density resulting from the combination of multiple scan tracks into larger multilayer specimens. Larger multilayer specimens with an outside dimension of 23 x 20 x 10 mm were also processed with an initial set of laser scan parameters, (termed “A”, selected for high densification) followed by various rescanning parameters (termed “B₁”, ..., “B_n”), selected to modify the sub-grain cell size. A single sample of each multilayer specimen with either uniform scanning or rescanning was produced. The rescanning process was carried out by first scanning a layer with the initial parameter A, and then rescanning the layer with parameter B following the same direction as initial scans. Scanning was rotated by 90 degrees between each layer. In order to study the effect of rescanning on microstructural heterogeneity, 1, 5, 10, and 20 layers of rescanned layers were processed in a single component, each separated by a constant spacing of 20-layers scanned with initial A parameters (Fig. 1). A stepped edge was used to identify each rescan region.

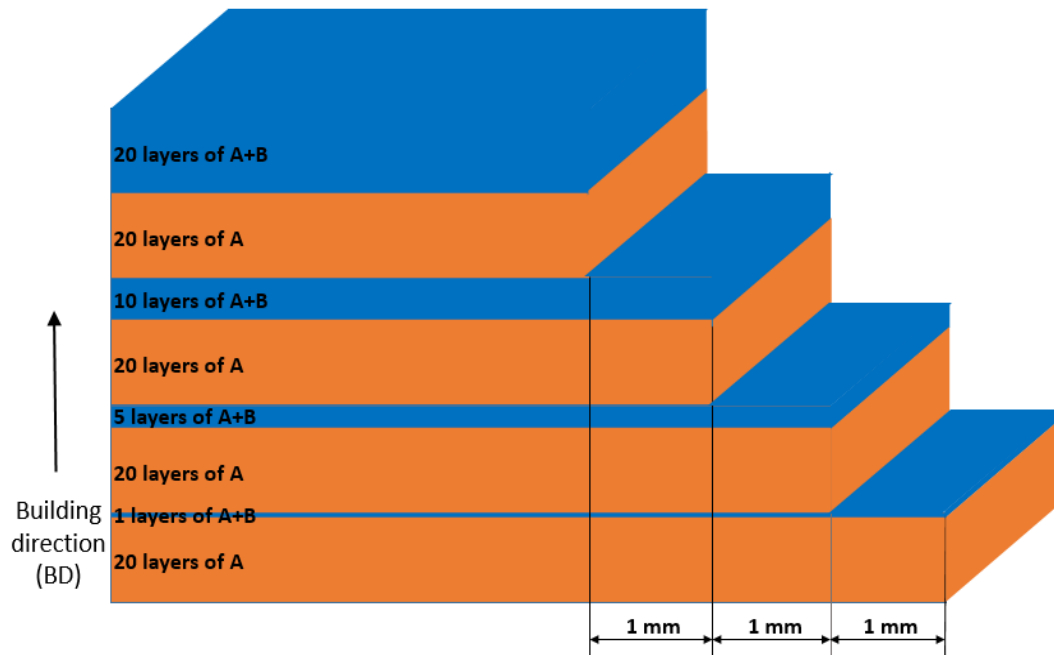


Figure 1 Cross sections of components containing 1, 5, 10 and 20 layers of rescanning. Orange represents tracks scanned uniformly by initial A parameter, blue represents the tracks scanned first by parameters A, and then rescanned by parameters B.

The dimensions of the melt pools (defined in Fig. 2) were measured using an Olympus BX41M-LED optical microscopy (OM) (Tokyo, Japan). For single laser scans, the average width of melt pools was measured from the top view at three positions for each track, and depth was measured from the cross-sectioned plane near the middle of each track. The height and surface profiles of single tracks were measured with an Alicona G4 InfiniteFocus using variable focus measurement capability. The sub-grain cellular structure within melt pools was observed using a Carl Zeiss Leo 1450VP scanning electron microscopy (SEM) with Oxford Instruments Energy Dispersive Spectrometer. The cell size was measured by the line method according to ISO 643:2017 (ISO, 2019) with averages and standard deviations calculated from 25 measurements at 5 random positions on one cross-section of one sample for each specimen type. Before cross-sectional observation, samples were cut by Mecatome T210 precision automatic micro-cutting machine, mounted in KonductoMet[®] Resin, which is a conductive thermosetting phenolic compound, ground using 120, 800, 1200,

and 4000 grits abrasive paper, and polished using 1 μm diamond paste to obtain mirror-like surface finish. To reveal the microstructures, the polished surface was etched by Kalling's No.2 reagent (50 mL HCl, 50 mL ethanol, 2 g copper chloride) for approximately 10 s.

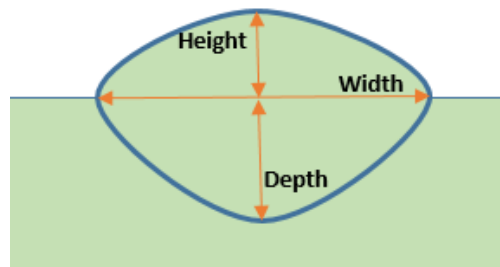


Figure 2 Schematic of single melt pool shape and dimensions, from side view.

The overall porosity of specimens was measured by Archimedes' method according to ASTM B962-17 (ASTM, 2017). Measurement of each sample was repeated five times to obtain averages and standard deviations. Local porosity in different initial or rescan regions was examined using OM after grinding and polishing, but before etching. Digital images were captured by OM and converted into a binary, black and white image. Threshold values were selected manually to enable identification of pores, and porosity was calculated as an area fraction of black to white pixels. The hardness measurement of the rescanned specimen in both initial scanning and rescanned regions was carried out by a Nanotest Vantage nanoindenter (Micro Materials Ltd) applied with a Berkovich tip where the indenter tip shape factor was taken into account in the analysis. Test were performed in accordance with ASTM E2546-15 (ASTM, 2015), in a load-controlled mode, the maximum indentation load was set to 60 mN and spacing between adjacent indentations was 40 μm . Averages and standard deviations were calculated from at least 10 measurements along a straight line in an initial

scanned region and 20-layer rescanned region. In the rescanned region, only indents within rescanned melt pools were included in the average.

2.2 Model for calculation of solidification parameters

2.2.1 Wilson-Rosenthal equation

The Wilson-Rosenthal equation is an analytical model of heat transfer to determine the 3D temperature field with a moving point heat source. In the past, this model has been applied to arc welding (Rosenthal, 1941). Hunziker et al. (2000) reported that at a sufficient distance from the laser source the temperature distribution obtained from the Wilson-Rosenthal solution for a point heat source can be used as an approximation of Eagar-Tsai's solution for a Gaussian distribution of energy around the center of the laser beam. The attractiveness of this model lies in its simplicity and low computational cost for very large numbers of points compared to fully numerical techniques. However, this model assumes steady-state conditions meaning that it cannot be used to predict the effects of complex beam paths and it cannot consider complex boundary conditions. Furthermore, the thermal properties (thermal conductivity, specific heat capacity) are assumed temperature-independent and the latent heat of solidification is neglected. The surface of the work piece is considered insulated (no radiative heat transfer) and convection within the melt pool at the heat source is neglected. Due to the similarity between LPBF and fusion welding, the Wilson-Rosenthal equation has been applied to predict the temperature field during LPBF processes by adding an assumption neglecting the effects of unfused metal powder at the surface of the work piece (Ye et al., 2018). Despite the simplifying assumptions, Scipioni Bertoli et al. (2019) validated use of the Wilson-Rosenthal equation for predicting cooling rates in LPBF processes with varying linear energy densities by reporting values in close agreement with both experimental measurements and with predictions based on

numerical modelling that included convective flow inside the melt pools and temperature dependent properties (Mukherjee et al. 2018).

The Wilson-Rosenthal equation predicts the three-dimensional, steady-state temperature field for a point heat source moving on a surface on the x - y plane orthogonal to the z -direction with a constant speed in the x -direction, as follows (Promopatum et al., 2017):

$$T = T_0 + \frac{P\varepsilon}{2\pi k\sqrt{x^2 + y^2 + z^2}} \exp\left[-\frac{v}{2\alpha}\left(x + \sqrt{x^2 + y^2 + z^2}\right)\right] \quad (2)$$

where T_0 is the initial temperature, P is the laser power, ε is the laser absorptivity, taken here as 0.58 as suggested for 316L SS by Rubenchik et al. (2015), k is thermal conductivity, v is the scanning speed, α is the thermal diffusivity, and $\sqrt{x^2 + y^2 + z^2}$ is the distance from beam location to the point of interest.

2.2.2 Temperature field calculation

Using Equation 2 and the thermal properties given in Table 3 for 316L SS at the melting point, the temperature fields during LPBF were calculated using *MATLAB*®. Temperature was calculated at points on a grid with spacings of 5 μm in length (x -direction), 2.5 μm in width (y -direction) and 0.5 μm in depth (z -direction). The grid size was selected such that it contained the entire melt pool. The melt pool boundary was identified as the isothermal line equal to the melting temperature, T_M . Melt pool depth was determined as the z -coordinate of the deepest point in the melt pool boundary. To simulate the temperature distribution of a single track with varying parameters, the solution was iterated for different combinations of laser power and scan speed given in Table 2. For multiple scans in multilayer specimens, the effect of previous adjacent laser scans was included by superposing the temperature field for an additional heat source located at a distance of the hatch spacing in the y -direction and the scan track length in the x -direction.

Table 3 Thermal properties for 316L SS used in Wilson-Rosenthal equation.

Property	Value	Unit	Reference
Room Temperature, T_0	25	°C	
Melting Point, T_M	1385	°C	(Mills, 2002)
Thermal Conductivity, k	12.45	W/mK	(Additive, 2019b)
Specific heat, c_p	468	J/kgK	(Additive, 2019b)
Thermal Diffusivity, α	3.4×10^{-6}	m^2/s	(Additive, 2019b)
Absorptivity, ε	0.58		(Rubenchik et al., 2015)

2.2.3 Solidification parameters calculation

The temperature gradient (G) was obtained from the calculated temperature fields using a central finite difference scheme. The solidification rate (R) was estimated as $v \cos(\beta)$, where β is the angle between the heat flow direction and the laser scanning direction calculated from $\tan(\beta) = G / G_x$, and G_x is the component of G in the x -direction (Bertoli et al., 2019). These relations assume steady-state scanning away from any boundaries or turns in the scanning direction. The cooling rate was determined as the product of the temperature gradient and solidification rate, $G \times R$. As suggested by Promopattum et al.(2017), a single value of the cooling rate was reported as the average of the values obtained along the melt pool boundary from the bottom of the melt pool to a distance of 30 μm (one layer height) above the bottom of the melt pool (towards the trailing edge). Distances above one layer height from the bottom of the melt pool were neglected from the average because they are expected to undergo remelting during subsequent depositions in multilayer scanning.

3. Results and discussions

3.1 Single-scan experiments

The melt pools from single laser scans processed as specified in Table 2 were classified into three representative morphologies: keyhole tracks (Figure 3 (a)), conduction mode (Figure 3 (b)), and discontinuous tracks (Figure 3 (c)), according to

depth-to-width aspect ratio (DWR). Eagar and Tsai (1983) reported that the cross section of a melt pool formed in conduction mode is approximately semi-circular so that $DWR \cong 0.5$. King et al. (2014) proposed that keyhole melting, caused by excessive energy penetration, can be identified by $DWR > 0.5$. Severe keyhole mode can cause porosity defects due to turbulent gas entrapment and melt pool vaporization (Saunders, 2017). Discontinuous tracks due to insufficient heat show a large variation in height along the scan track and sometimes drop below the base plate under the powder layer, which may cause the incomplete fusion and bonding between adjacent tracks and layers, and therefore induce porosity defects.

The dimensions (width and depth) of melt pools from single laser scans and the variation of melt pool dimensions with energy density are shown in Figure 4 for selected parameters from Table 2 with the same value of P/v . Linear energy density, defined as P/v , can be used to quantify energy per unit length for single laser scans, rather than energy per unit volume since hatch spacing is not defined and layer thickness is constant. For each laser power except 50 W, the width and depth of melt pools increased with increasing energy density due to larger input energy, which is consistent with other reports (Matilainen et al., 2014). Melt pools processed with a laser power of 50 W deviated from this trend in width because low laser power was more likely to form discontinuous tracks due to insufficient energy density (Figure 3 (c)).

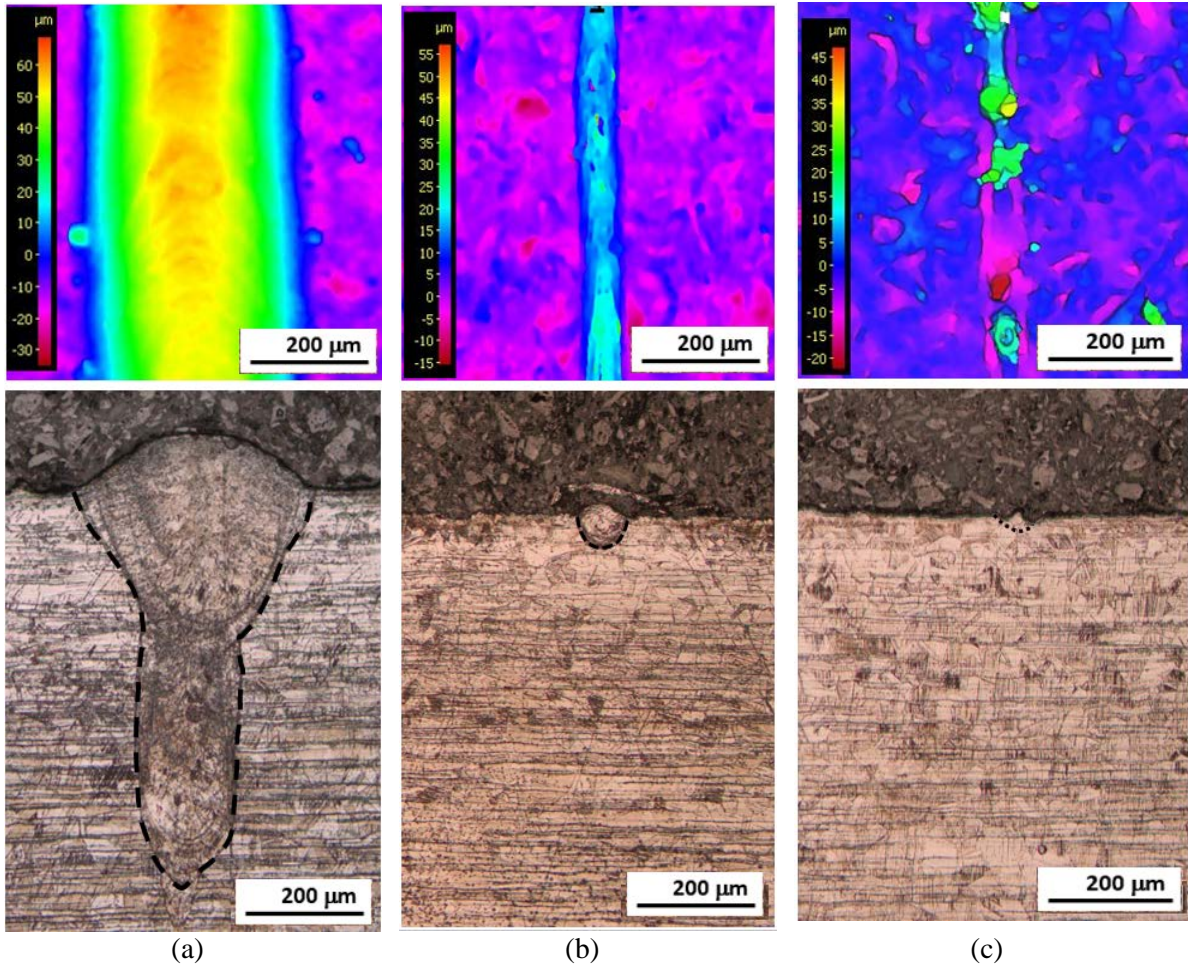


Figure 3 Top views of height profiles (top row) and side views of cross-sectioned melt pools (bottom row) representative of (a) continuous melt pool in keyhole mode ($P = 200$ W, $v = 50$ mm/s, $P/v = 4$ J/mm); (b) continuous melt pool in conduction mode ($P = 150$ W, $v = 1200$ mm/s, $P/v = 0.25$ J/mm); (c) discontinuous melt pool ($P = 150$ W, $v = 3200$ mm/s, $P/v = 0.05$ J/mm). The boundaries of the melt pools are indicated with black dash lines.

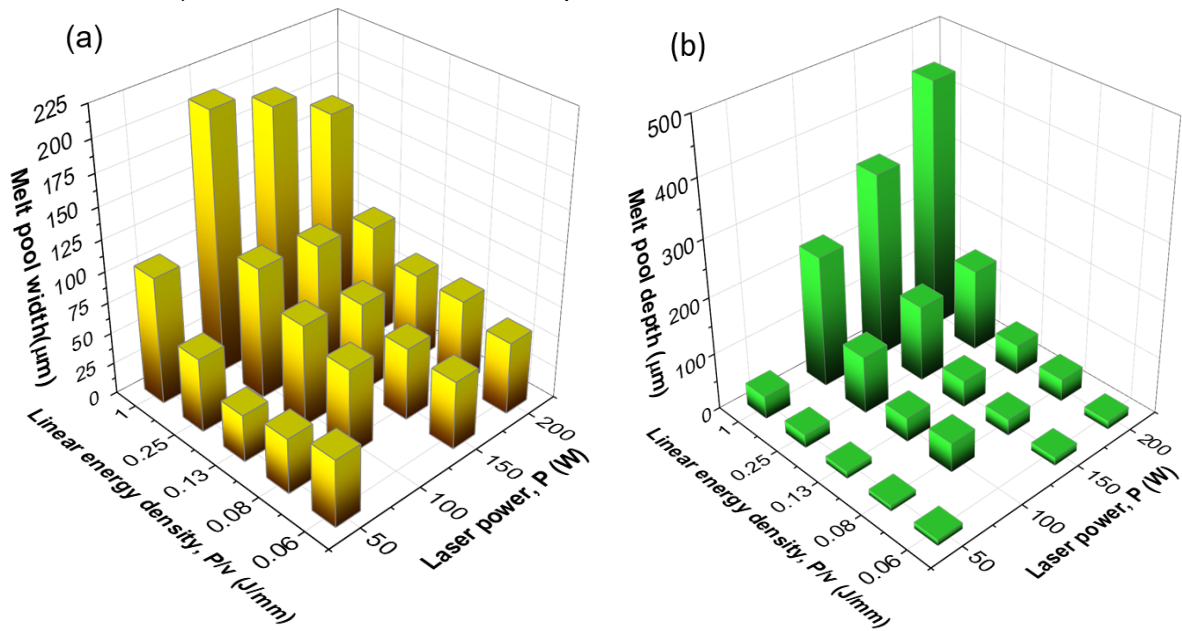


Figure 4 (a) Average width and (b) depth of single laser scan tracks with different linear energy densities and laser powers. The range in measurements was up to 21.9% of widths and 27.9% of depths.

A sub-grain dendritic/cellular structure was observed within the melt pools, as shown in Figure 5. In Fig. 5 (a), grains (outlined in blue) are radially oriented within the melt pool and elongated in the direction of solidification, which is perpendicular to the melt pool boundaries, as reported by Casati et al. (2016). Fig. 5 (b) shows that each grain contains a colony of sub-grain cellular dendrites oriented in the same direction as the grains. By varying LPBF process parameters, the cell size changed due to variation in solidification rate caused by different linear energy density, as shown in Figure 6 for selected parameters from Table 2 with the same value of P/v . With a constant laser power, cell size increased with increasing P/v values (due to decreasing scan speed), which can be attributed to lower cooling rate within melt pools (Clymer et al., 2017).

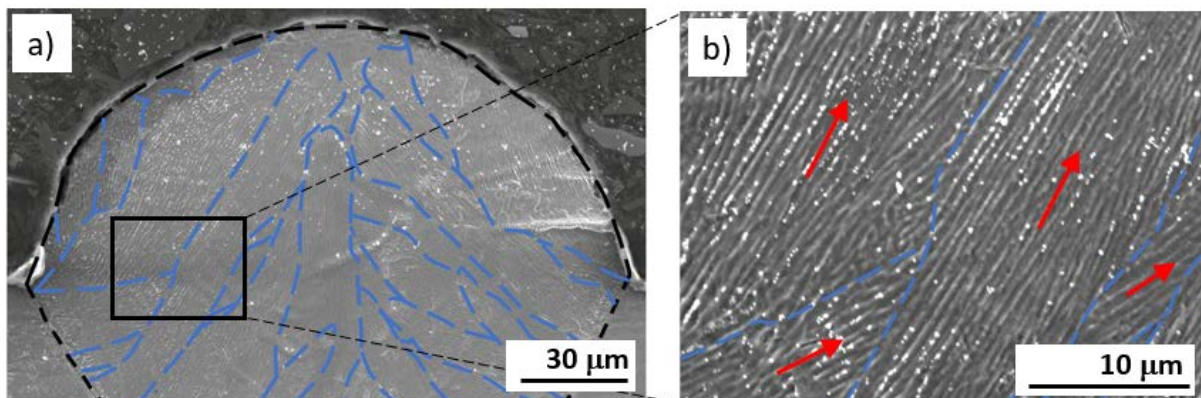


Figure 5 SEM images of single laser scan tracks showing (a) grains and (b) sub-grain cellular dendrite structure. The melt pool boundary is marked by a black dash line, blue dash lines mark grain boundaries, and red arrows indicate the growth direction of cellular dendrites.

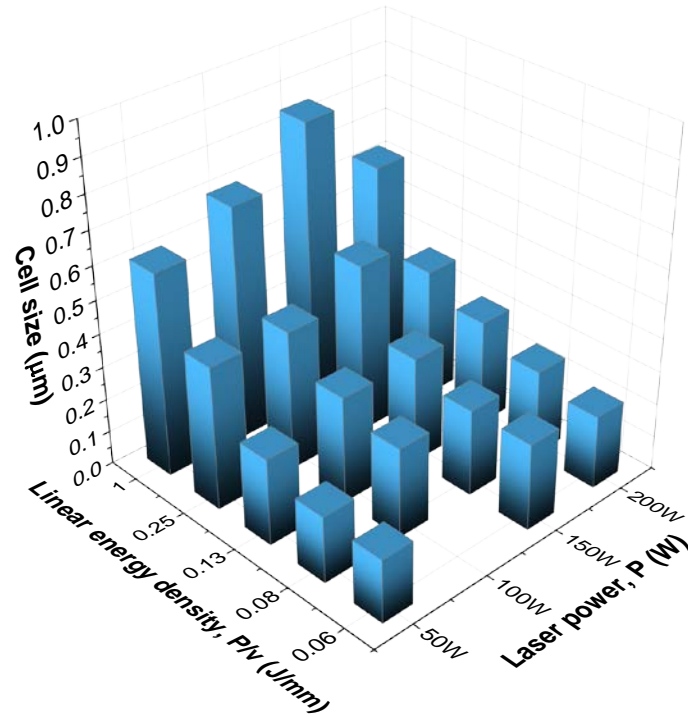


Figure 6 Cell size of single laser scan tracks with different linear energy density and laser power. The range in measurements was up to 26.9%.

A P - v plot (Figure 7) summarizes the morphology and sub-grain cell size of single scan tracks. Both cell size and DWR were higher in regions where linear energy density (P/v) is higher, indicating that with increased energy, melt pools became deeper and sub-grain cellular structure became coarser due to a slower cooling rate, while lower P/v resulted in discontinuous tracks due to insufficient energy input, which is consistent with literature from Guo et al. (2018). The regions of continuous tracks with $DWR < 1$ are likely to achieve LPBF components with a high level of density. In these regions (yellow and blue), the largest and smallest average cell sizes measured were $0.85 \mu\text{m}$ and $0.26 \mu\text{m}$, respectively.

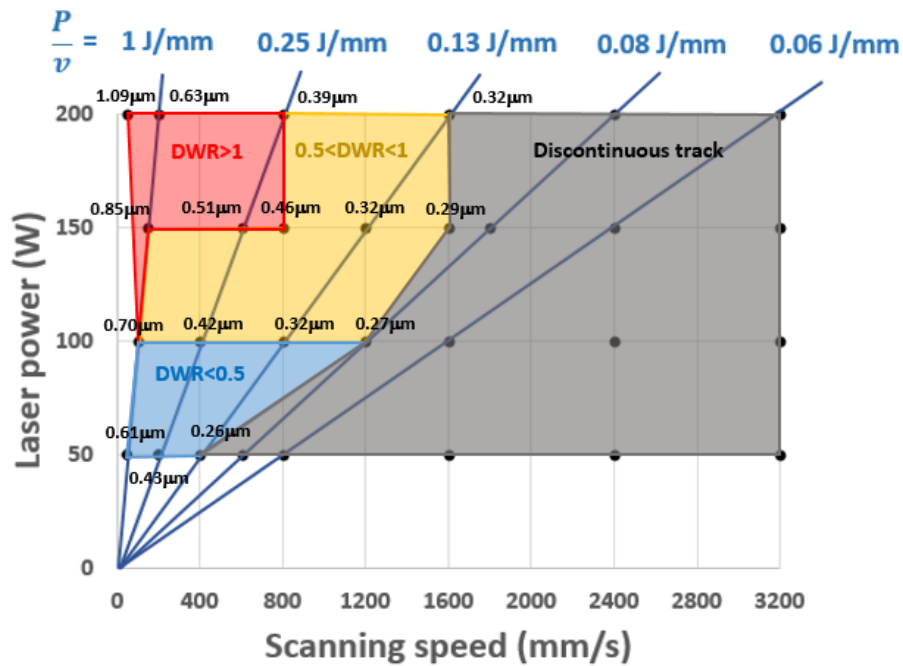


Figure 7 Laser power-scan speed, P - v , plot summarising morphology and sub-grain cell size of tracks with varying processing parameters. Regions of severe keyhole tracks ($DWR > 1$), slight keyhole tracks ($0.5 < DWR < 1$), and discontinuous tracks are marked in red, yellow, and gray shading, respectively. Average cell size is specified above each data point.

3.2 Single-scan simulation

After the temperature field was obtained from Wilson-Rosenthal equation, the melt pool boundary of single-scan melt pool was obtained as the locations where the temperature was predicted to drop below the melting point. The predicted melt pool depth (black points) as a function of linear energy density is shown in Figure 8 and compared with measured depth from experiments at 200 W, 150 W, 100 W, and 50 W (blue, orange, grey, and yellow rectangular points). Although the predicted trend of increasing depth with increasing P/v matched experimental results, predictions for individual sets of processing parameters were not accurate in most cases due to the assumptions of this modelling, which results in predicted melt pool shape with constant $DWR=0.5$. Only a minority of melt pools in conduction mode were experimentally observed to have a shape with DWR of 0.5. At lower linear energy densities, the measured depth was smaller than the predicted depth because of the shallow melt

pool and discontinuous tracks; conversely, at higher linear energy density, the experimental results were larger than the predicted depth due to keyhole mode.

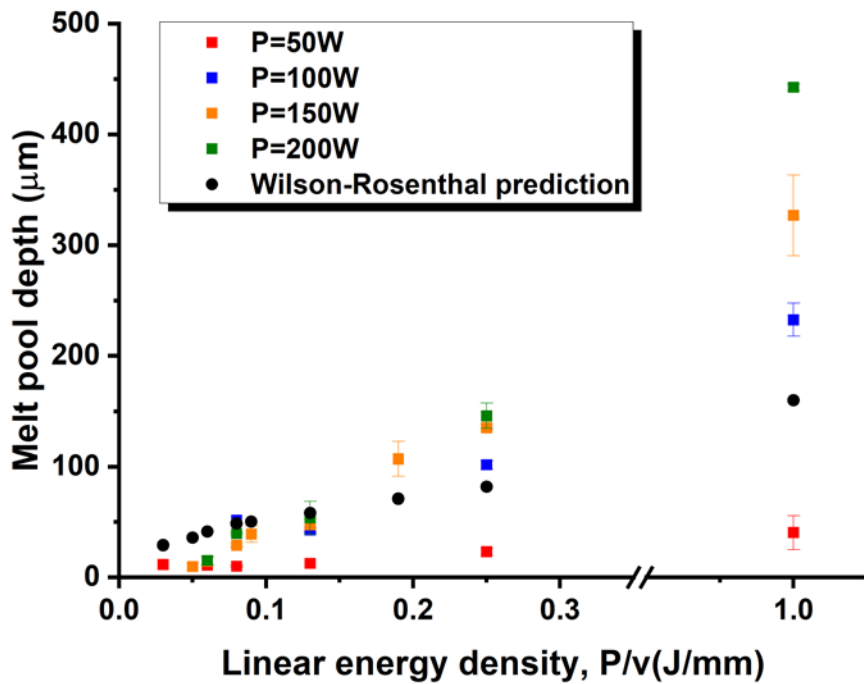


Figure 8 Predicted and measured depths of melt pools from single laser scans as a function of the linear energy density, P/v . Error bars bound one standard deviation.

The predicted cooling rates $G \times R$ from the 29 sets of parameters (Table 2) are plotted in Figure 9 with respect to linear energy density (P/v), which was found to be inversely proportional to the P/v , as expected. Fewer than 29 data points are visible in Figure 9 because parameters with the same or similar P/v are overlapping. The data were fitted using a power law, yielding the relationship between linear energy input and cooling rate in Equation 3:

$$G \times R = 1.6 \times 10^5 \left(\frac{P}{v}\right)^{-1.182} \quad (3)$$

The exponent of the fitted power law indicates that cooling rate is close to linear proportionality with the inverse linear energy density, v/P . Similar predictions obtained by Scipioni Bertoli et al. (2019) are also shown in Figure 9. The deviation between these curves can be explained by the different absorptivity values used, 0.58 for this study and 0.35 for the others. The value of laser absorptivity in this work was selected

as 0.58 because Rubenchik et al. (2015) performed a direct measurement of absorptivity on 316L SS powder and reported that absorptivity was practically independent of temperature and heating rate at two different power inputs. Other work has reported fluctuations in absorptivity of 316L SS powder ranging from approximately 0.3 to 0.6 for stable melt pools (below threshold for keyholing), depending on the laser power and scan speed (Trapp et al., 2017), but these potential variations were not considered here in this work. In addition, an analytical expression obtained from Wilson-Rosenthal's equation for the cooling rate of a point along the laser travelling direction provided by Kistler et al. (2017) also gave an inverse relationship with linear energy density (Equation 4):

$$\frac{dT}{dt} = 2\pi k \frac{v}{\varepsilon P} (T_m - T_0)^2 \quad (4)$$

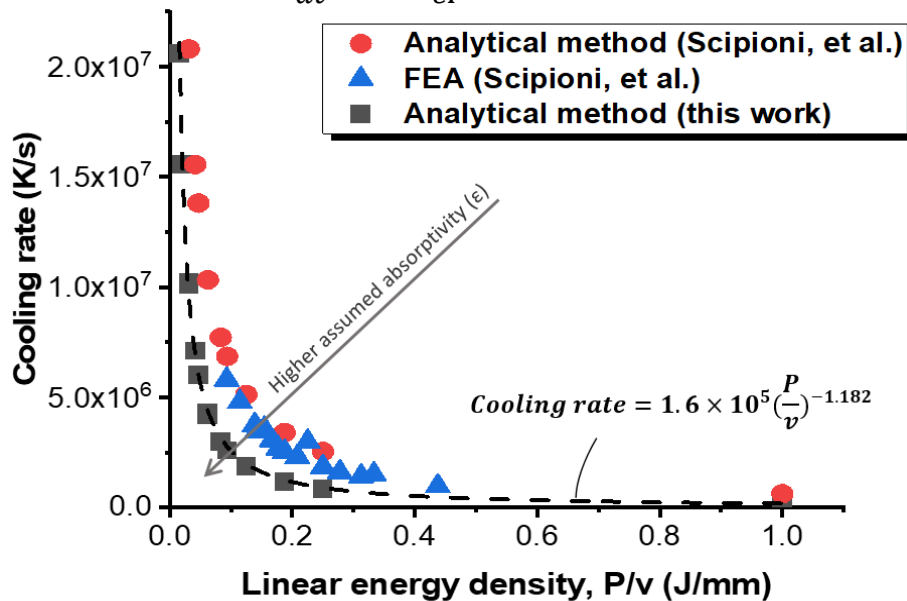


Figure 9 Cooling rate, $G \times R$, expressed as a function of the linear energy density, P/v .

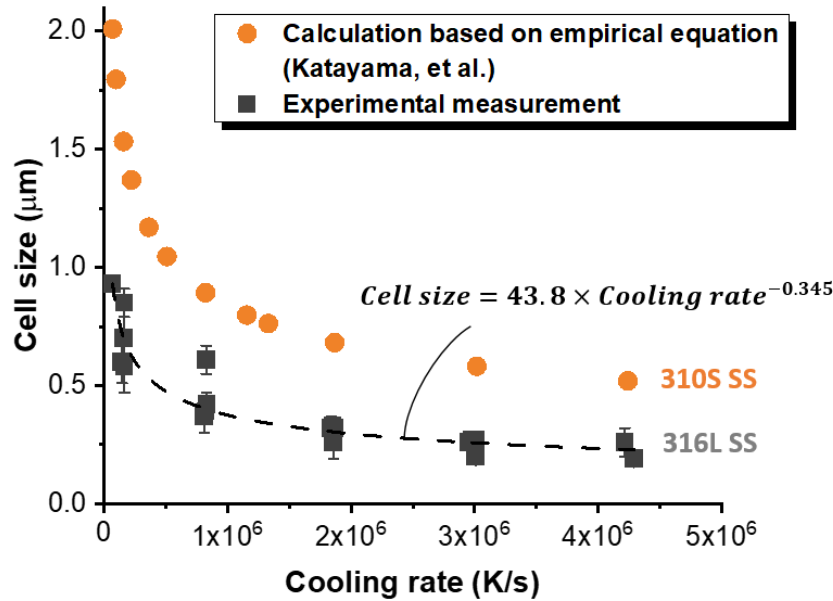


Figure 10 The experimentally measured cell size obtained with CL M2 printer and calculated cell size based on empirical equations are shown as a function of predicted cooling rate. Error bars bound one standard deviation.

A study by Katayama and Matsunawa (1984) correlated cell size (d) with cooling rate ($G \times R$) for austenitic stainless steels, with an equation (Equation 5) in the general form:

$$d = A \cdot (G \times R)^n \quad (5)$$

where A and n are constants related to the materials. Also, in their study, an empirical equation was obtained for 310S SS (Equation 6):

$$d = 80 \cdot (G \times R)^{-0.33} \quad (6)$$

The measured cell sizes of 316L SS (black points) from single-scan experiments at corresponding predicted cooling rates are shown in Figure 10 and compared with values from the empirical equation for 310S SS (orange points). The predicted trends are similar for these two steels, with differences potentially attributable to the different compositions, and to the different methods used to estimate cooling rate (estimated based on correlations with thermocouple measurements in cited work on 310S SS). Therefore, the power law fit for measured cell size as a function of cooling rate for 316L SS from is given as Equation 7:

$$d = 43.8 \times (G \times R)^{-0.345} \quad (7)$$

Combining Equation 3 and 7, a direct relationship between linear energy density and cell size was obtained as Equation 8:

$$d = 0.7 \times \left(\frac{P}{v}\right)^{0.41} \quad (8)$$

3.3 Multilayer part fabrication

From the results of single laser scan experiments, five sets of parameters were chosen and listed in Table 4 in descending order of cell size (from 0.85 μm to 0.26 μm) measured in single laser scans. To enable manufacture of parts with a large difference in cell size, and therefore large expected differences in hardness and strength, two parameters corresponding to maximum (A1, A2) and one for minimum cell size (A5) were selected from the boundaries between severe keyhole region and slight keyhole region, and the boundaries between continuous and discontinuous regions as shown in Figure 7. Two parameters in region of $DWR < 1$ with intermediate cell sizes were also chosen (A3, A4). In order to avoid lack of fusion defects between adjacent scans, the hatch spacings in Table 4 were chosen as 70% of the expected track width based on single scan tracks (resulting in 30% overlap between adjacent scans) (Di et al., 2011).

Table 4 Processing parameters used for multilayer specimen manufacture.

Parameter number	A1	A2	A3	A4	A5
Cell size from single scans (μm)	0.845	0.700	0.320	0.316	0.258
Laser power, P (W)	150	100	150	100	50
Scan speed, v (mm/s)	150	100	1200	800	400
Hatch spacing, h (μm)	133.5	145.3	50.8	57.1	26.5
Energy density, E (J/mm^3)	249.69	229.41	82.02	72.97	157.23
Linear energy density, P/v (J/mm)	1	1	0.13	0.13	0.13

The density of multilayer cubes was measured by both Archimedes method and OM and are compared in Figure 11. A target density level of 99% for little or no impact on quasi-static mechanical properties, assuming nearly spherical low aspect ratio pores (Yusuf et al., 2017), is indicated by a red dashed line. The density measured from OM was 1.59% – 3.99% higher than the density from Archimedes method, but the Archimedes method was considered more reliable as the whole sample volume was taken into account instead of discrete cross sections, which may not represent an overall porosity of the sample. Furthermore, the standard deviation of the Archimedes method (< 0.35%) is lower than for OM (< 1.41%), especially for parts with lower densities. The higher density determined by OM might be attributable to pores with a size smaller than or close to the resolution of the microscope, which may not be captured by the thresholding procedure used in the image analysis of density. Comparing the density of cubes measured by OM method, cubes processed with parameters A1 and A2 (with highest energy densities of 249.69 J/mm³ and 229.41 J/mm³) showed highest densities of 99.6% and 99.9%, while cubes with parameters A3 and A4 (processed with lowest energy densities of 82.02 J/mm³ and 72.97 J/mm³) had lower densities of 97.0% and 96.4%. Despite a higher energy density than cubes A3 and A4, cube A5 (157.23 J/mm³) exhibited the lowest density of 91.2%, possible reasons for which are discussed below.

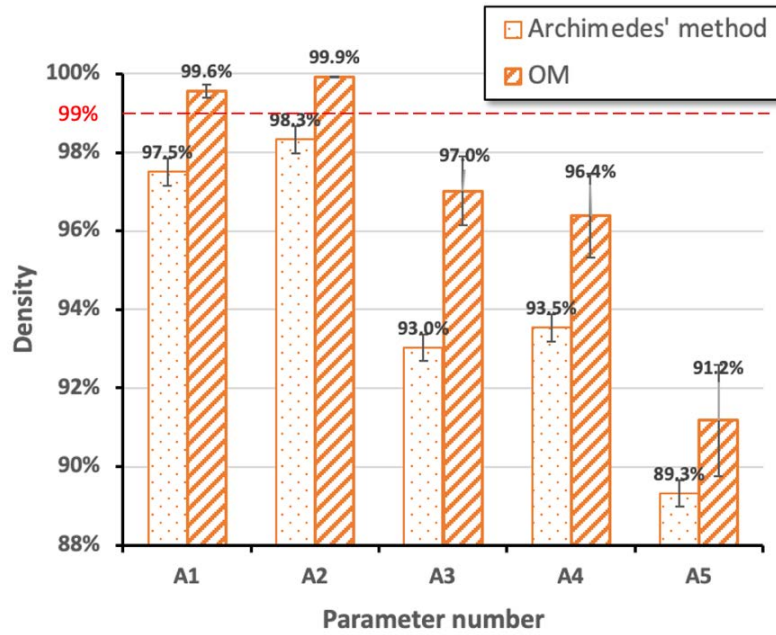
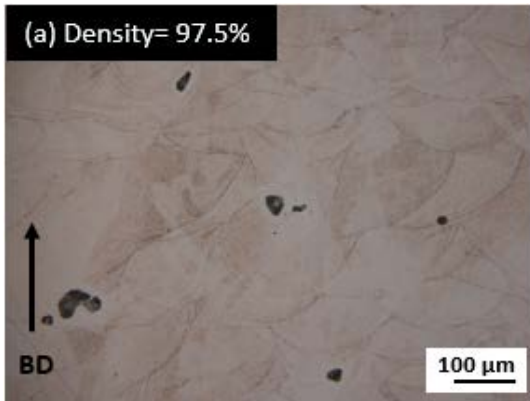
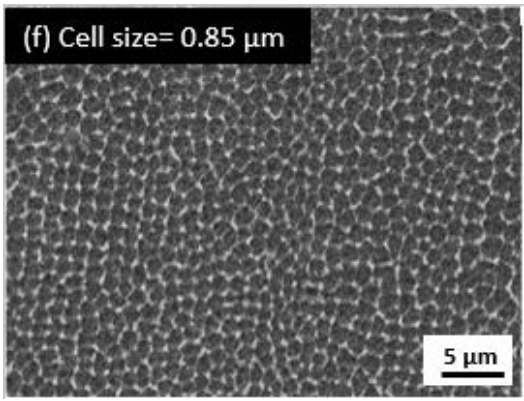
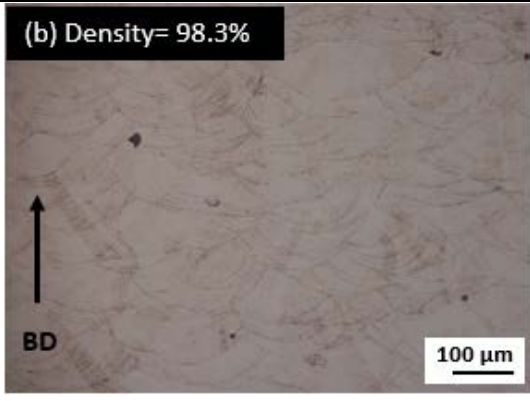
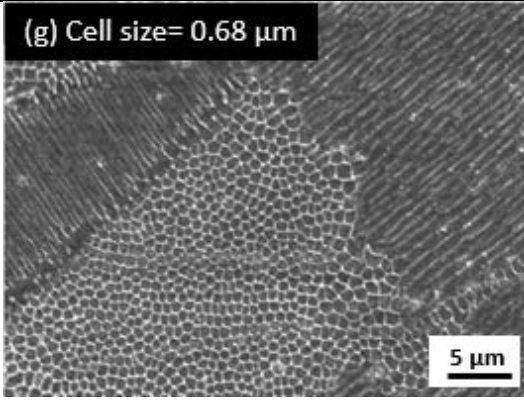
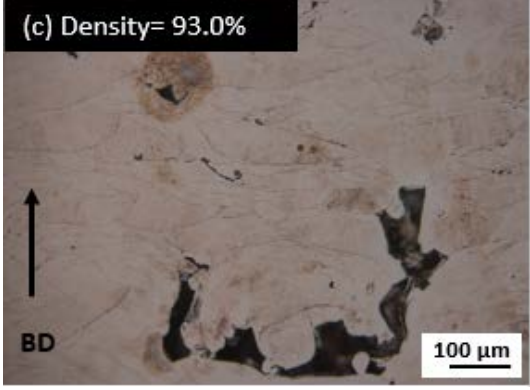
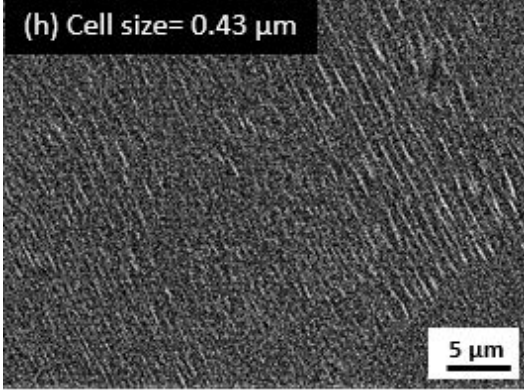


Figure 11 Density of five cubes produced via different processing parameters measured by both Archimedes method and optical microscopy. Error bars bound one standard deviation.

The shapes and distribution of pores within multilayer specimens processed with each different parameter are displayed in Fig. 12 (a) – Fig. 12 (e). As shown in Fig. 12 (a) and (b), pores in cubes A1 and A2 (with highest energy densities of 249.69 J/mm^3 and 229.41 J/mm^3) were mostly spherical in shape and small in size, and mostly distributed within melt pools. This suggests the pores were gas-induced by high laser energy, turbulent melt pool dynamics, vaporization of low melting point constituents (Zhang et al., 2017) or gas-induced voids embedded within the powder feedstock (Hao et al., 2009). However, cubes A3, A4, and A5 (with lower energy densities than cubes A1 and A2) showed irregular, non-spherical and larger pores, suggesting process-induced porosity formed by insufficient melting or lack of fusion between adjacent scan tracks and/or successive layers (King et al., 2014). The pores in cube A3, A4, and A5 (Fig. 12(c–e)) were mainly located beneath the boundaries of the melt pools and some un-melted powders were observed adjacent to a triangular void, which suggests lack of fusion due to insufficient energy density input. Although cube A5 had a higher energy density (157.23 J/mm^3) than cubes A3 and A4 (82.02 J/mm^3 and 72.97 J/mm^3),

~4% lower density was exhibited. This can be explained by the discontinuous melt pools produced in single laser scans using the A5 parameters, which would lead to inconsistent overlap between adjacent scans, and a melt pool size (height plus depth of 29.2 μm) slightly smaller than the powder layer thickness of 30 μm .

Parameter No.	Pores shape	Sub-grain structure
A1 $\frac{P}{v}=1$ J/mm	(a) Density= 97.5% 	(f) Cell size= 0.85 μm 
A2 $\frac{P}{v}=1$ J/mm	(b) Density= 98.3% 	(g) Cell size= 0.68 μm 
A3 $\frac{P}{v}=0.13$ J/mm	(c) Density= 93.0% 	(h) Cell size= 0.43 μm 

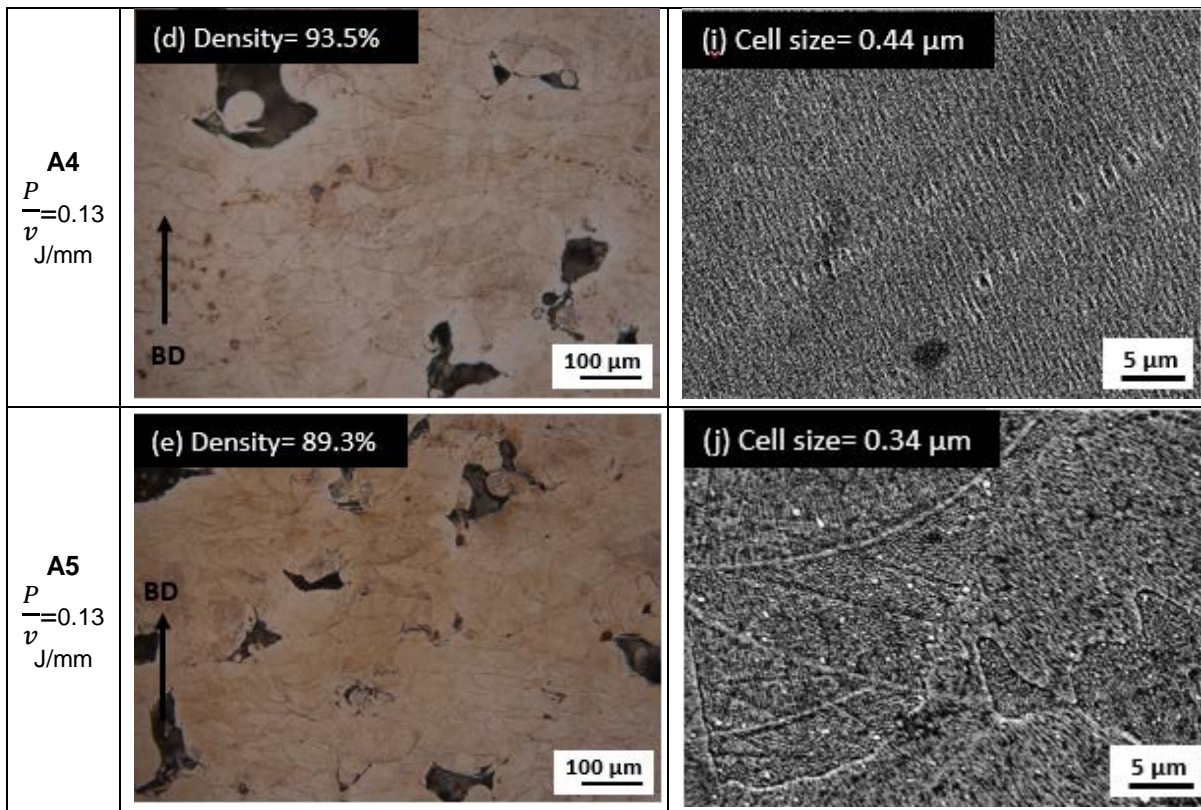


Figure 12 Pore morphology and sub-grain structure for five cubes processed using parameter A1–A5, as indicated.

The sub-grain cellular structures of multilayer specimens are shown in Fig. 12 (f–j), and the average cell size is given on each corresponding image. Building direction (BD) is also indicated. With decreasing P/v from 1 to 0.13 J/mm, the cell size decreased from ranges of 0.68–0.85 μm to 0.34–0.45 μm . These average values with standard deviations (orange points) are shown in Figure 13. This figure also shows the predicted cell size of multilayer tracks obtained from the Wilson-Rosenthal equation and the empirical relationship in Equation (8) (grey points), as well as the measured cell size from single scan track experiments (black points). Results for single scans and multilayer specimens cannot be distinguished for A1 in Figure 13 because the similar average values are overlapping. Across all parameters, the average cell size for single scans and multilayer scans do not appear significantly different, and a paired t-test supports this observation (P -value of 0.11 obtained from a two-tailed paired t-test indicates the null hypothesis, that there is no difference

between cell sizes, cannot be rejected (King and Eckersley, 2019)). The Wilson-Rosenthal model predictions again showed good agreement with experimental measurements of cell size in both single tracks and multilayer cubes.

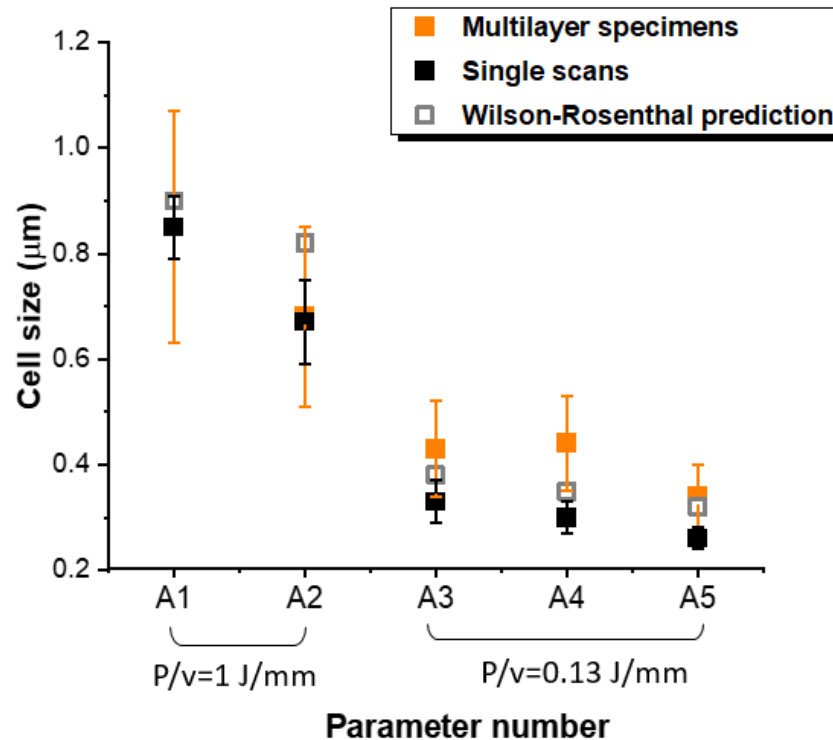


Figure 13 Cell size for five cubes processed using parameter A1–A5, as indicated. Error bars bound one standard deviation.

3.4 Multilayer fabrication with rescanning

Without rescanning, little variation in cell size (0.68–0.85 µm) was achieved while maintaining high densities (>97.5%) for multilayer parts (i.e. cubes processed with parameters A1 and A2, Table 4 and Fig. 11, 12). Therefore, initial scanning was implemented to achieve high densification, with rescanning using different laser parameters to achieve a larger variation in cell size. The parameter A1 was selected as the initial parameter (Parameter A) for high densification (> 97.5%) and a coarse cell size of 0.85 µm. Rescanning parameters (B_n parameters) with finer cell sizes were selected to achieve large differences in cell size in initial and rescan regions. Based on results from the P - v plot in Figure 7, rescanning parameters were selected from the

boundaries between continuous tracks and discontinuous tracks for small cell size, as listed in Table 5 (Note: B1 parameters are the same as parameter A5 in Table 4).

Table 5 Parameters for rescanning experiment.

	A	B1	B2	B3	B4
Cell size from single scan (μm)	0.845	0.258	0.323	0.291	0.273
Laser power, P (W)	150	50	200	150	100
Scan speed, v (mm/s)	150	400	1600	1600	1200
Hatch spacing, h (μm)	133.5	42.8	80	39.6	53.3
Energy density, E (J/mm^3)	249.69	97.35	52.08	78.91	52.12
Linear energy density, P/v (J/mm)	1.00	0.13	0.13	0.09	0.08

Melt pools in different regions with either 1, 5, 10 or 20 layers of rescanning (specimen detailed in Fig. 1) are shown in Figure 14 for A+B4 initial+rescan parameters. Rescanned melt pools were identified by the difference in contrast after etching, as confirmed by the refined cell size measured from SEM images. For 1-layer of rescanning (Fig. 14(a)), the rescanned melt pools (marked in blue lines) were mostly covered by the next layer of initial scanning melt pools (shown in orange lines) so that the proportion of refined microstructure within the layer from rescanning was small. With increasing layers of rescanning, as shown in Fig.14 (c) and (d), the proportion of rescanned melt pools within layers appeared to increase and were arranged more continuously along layers. This might be explained by the expected effect of rescanning on surface quality and reduced roughness (Ra decreases from $12 \mu\text{m}$ down to $1.5 \mu\text{m}$ has been reported by Yasa and Kruth (2011)). A flat surface with a smaller surface roughness can help next layer of metal powder to spread with a more uniform thickness, t . More uniform powder layers lead to more uniform melt pool sizes because the volumetric energy density is more uniform (it is inversely related to t ,

Equation 1) and because the boundary conditions for heat transfer from the solidifying melt pool to the surrounding layers are more uniform.

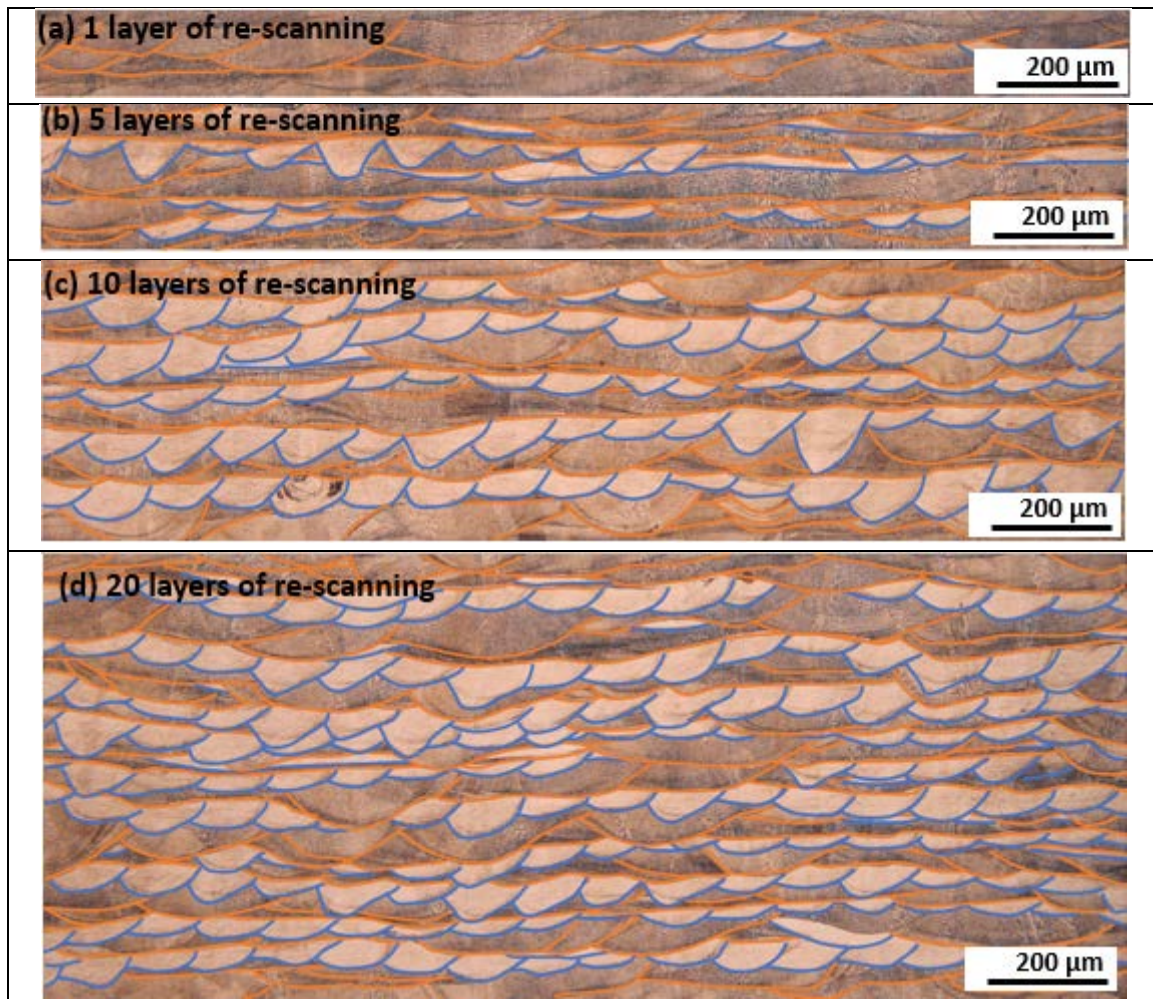


Figure 14 Comparison of melt pool distribution after 1, 5, 10, and 20 layers with rescanning using parameters A+B4. Blue lines indicate rescanning melt pool boundaries from parameter B4 and orange lines represent melt pool boundaries of initial scanning with parameter A.

The sub-grain microstructure in initial and rescanned regions were investigated in regions with 20 layers of rescanning for each combination of A and B_n. As shown in Figure 15, the local densities of regions with 20 layers of rescanning (A+B1, A+B2, A+B3, and A+B4) were measured by OM and compared with the density (also measured by OM) of the uniform specimen processed with initial parameter A (Parameter A1 from Figure 11). All rescanning regions had densities between 0.27–0.41% higher than the specimen processed with initial parameter A only. Similar

results were also reported by Yasa et al. (2011) who found porosity reduced from 0.77% to 0.036% with rescanning. Parameters B1, B2, B3, and B4 were all selected from the P - v plot in Figure 7 along the boundary with the region where discontinuous tracks were formed due to low energy density, and thus lack of fusion defects can be expected due to incomplete overlap between adjacent layers and tracks. Nevertheless, these parameters helped to improve the densification when used as rescanning parameters. For example, parameter B1 ($P = 200$ W, $v = 400$ mm/s) increased the density in the rescanning region from 99.55% to 99.96%, but as initial scan parameter A5 (with the same $P = 200$ W, $v = 400$ mm/s) the density was only 91.2% (Figure 11) and the microstructure showed high porosity and large irregular lack of fusion pores (Figure 12 (e)). This density improvement can be attributed to the re-melting caused by rescanning, which enables gas pores to escape from the liquid-state melt pool. The small size and overlap between melt pools that causes lack of fusion when initially scanning raw powder does not induce pores when rescanning solidified melt pools.

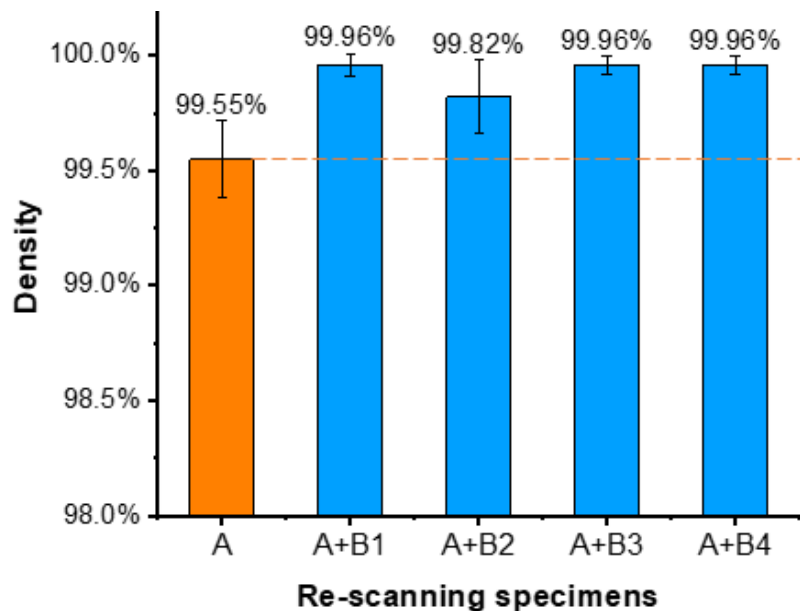

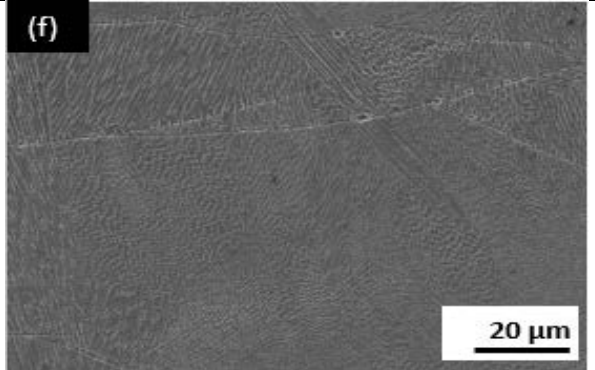
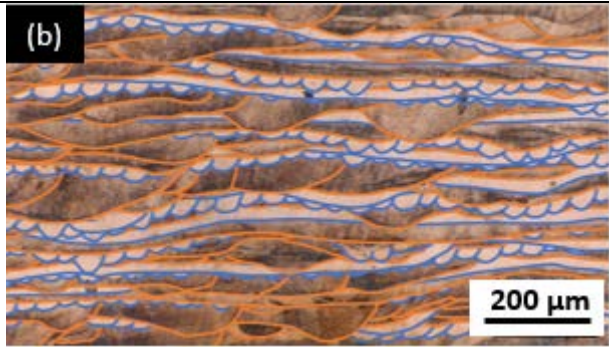
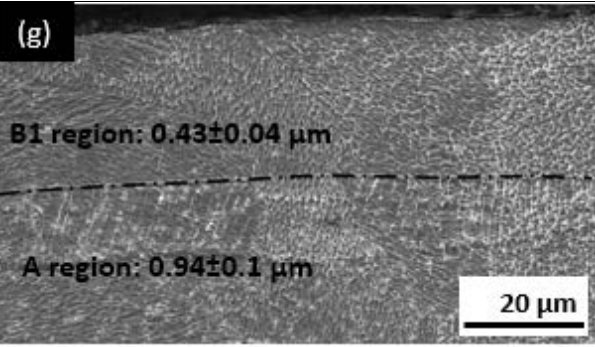

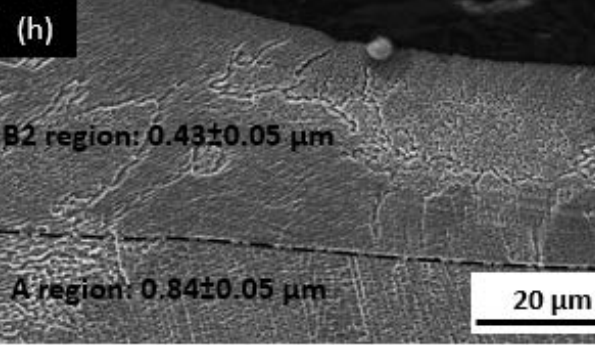


Figure 15 Optical micrograph measurements of local density at regions with 20 layers of rescanning in specimen A+B1, A+B2, A+B3 and A+B4 compared with a uniform sample processed with initial parameter A only. Error bars bound one standard deviation.

The melt pools in regions with 20 layers of rescanning for A+B1, A+B2, A+B3, and A+B4 are shown in the first column of Figure 16 (a–e). Within the rescan regions, sub-grain cell size was measured both in melt pools resulting from the initial A parameters and in melt pools from B_n parameters, as presented in the second column of Figure 16 (f–j). After applying rescanning with the four selected parameters, all rescan regions showed a refined sub-grain cell size.

Parameters	Melt pool	Sub-grain cellular structure
A $\frac{P}{v}=1$ J/mm		
A+B1 $\frac{P}{v}=0.13$ J/mm		
A+B2 $\frac{P}{v}=0.13$ J/mm		

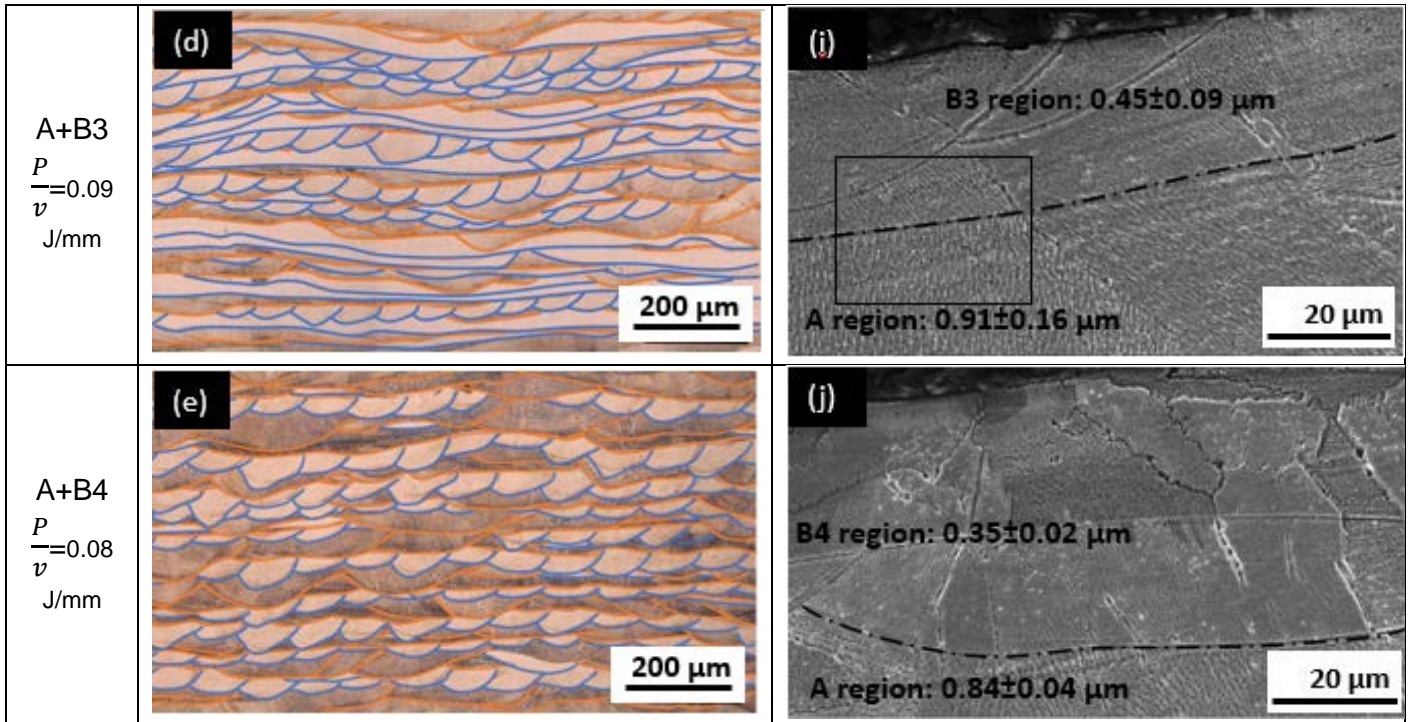


Figure 16 Melt pools in regions initially scanned with A (a–e) and rescanned with B_n parameters (b–e). Blue lines show rescanned melt pools and orange lines show initial scan melt pools. Corresponding sub-grain cellular structure (g–j), with black dashed line indicating the boundaries between initial and rescanned melt pools, and average cell sizes \pm one standard deviation. Box inset in (i) is shown in Fig. 17.

The transition from finer to coarser sub-grain regions in specimen A+B3 is shown in Fig. 17 (a detail of the inset box region shown in Figure 16(i)). At the interface between the refined rescan melt tracks (blue) and coarser initial scan melt tracks (orange) there is no apparent gradation in cell size, and the transition from coarse to finer across the melt track boundary appears to be sharp at this magnification. Therefore, the spatial distribution of cell size refinement is approximately equal to the size of the melt pools from rescanning (marked by blue lines in Fig. 16 (a–e)).

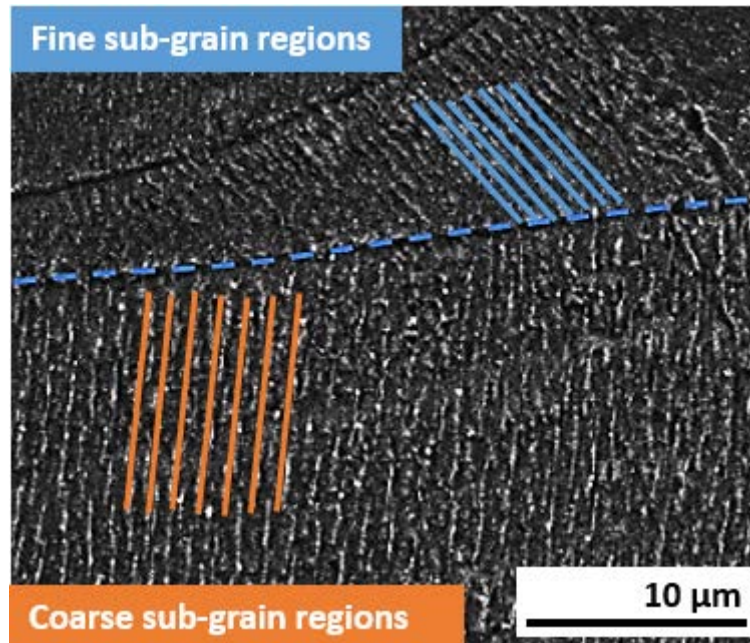


Figure 17 Transition from fine to coarse cell sizes at a melt pool boundary (dashed blue line) between initial scan parameters A (orange) and rescan parameters B3. Cellular structure spacings are highlighted with parallel lines in each region.

Figure 18 shows the measured cell size in both initial scanning regions (orange points) and rescan regions (blue points). Cell size measured from single scans with B1, B2, B3, B4 parameters are also marked (black points) as a comparison. The cell size in regions only scanned with initial parameter A was 0.75–1.07 μm, similar to the cell size measured in cube A1 (0.85 μm, Fig. 12). Compared with cell size obtained in single scans, rescanning regions show a similar but slightly larger cell size, likely due to the slower cooling and added heat from adjacent scan tracks. Among the rescanning parameters, parameter B4, with the lowest linear energy density, resulted in the smallest refined cell size (0.35 μm), and the largest difference in cell size between initial scanning region (0.84 μm) and rescanning region (0.35 μm). The Wilson-Rosenthal equation and the empirical relationship in Equation (8) were also applied to predict the cell size in rescanning region and showed good agreement with experimental results. The nano-hardness of the A+B4 rescanned specimen in both initial scanning and rescanned regions was also measured. Rescanned hardness data

were only taken from indents within rescanned melt pools, which were identified after indentation by microscopy. Compared with the region of initial scanning A, rescanning with B4 only showed a small, apparently insignificant increase in the average hardness values from 2.87 ± 0.11 GPa to 3.05 ± 0.09 GPa. Li et al. (2020) also reported a lack of correlation between cell size and hardening and argued that increasing dislocation density explains increases in hardness and strength of LPBF 316L SS, rather than cell size. An additional explanation for the insignificant effect on hardness may be the potential effects of rescanning on dynamic recrystallization and recovery, not only solidification (Sabzi et al., 2020). Thus, the potential for localised hardening and strengthening together with localised cell size refinement remains unclear and further work is needed to investigate dislocation density and these other potential effects of complex repeated heating cycles.

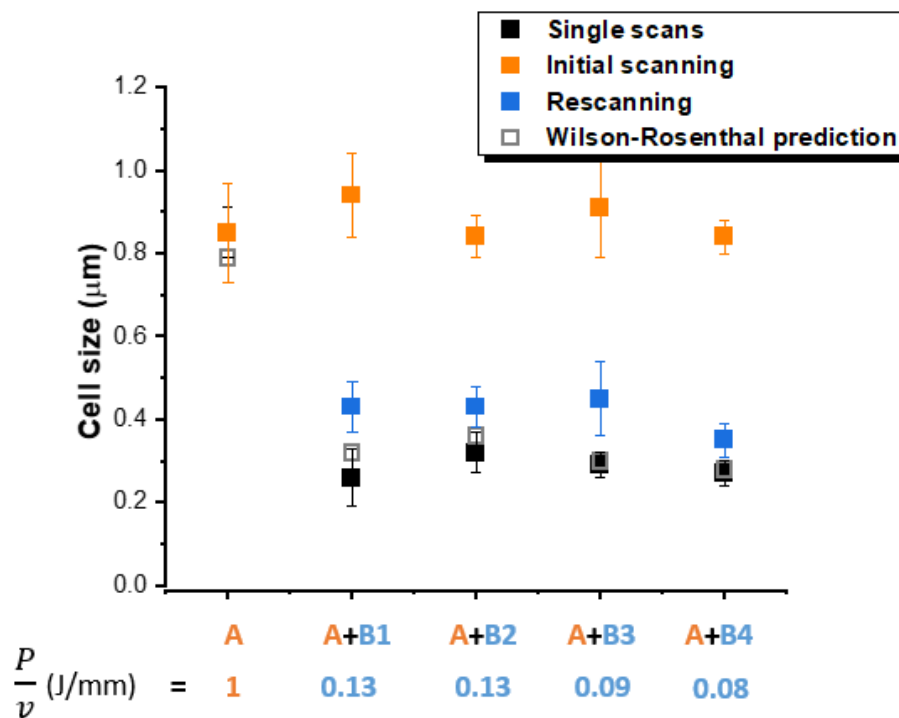


Figure 18 Measured and predicted cell sizes for both initial scanning and rescanning regions using parameter A+B1, A+B2, A+B3, A+B4. Error bars bound one standard deviation.

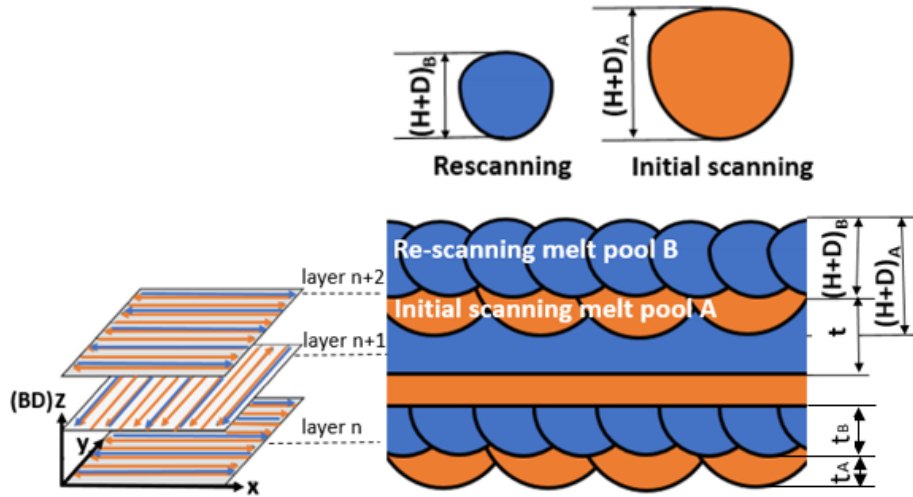


Figure 19 Schematic of rescanning strategy (left) and cross-sections of melt pools (right). Orange scans represent scanning with initial A parameter. Blue scans represent rescanning with B parameters.

Figure 19 shows a schematic of the rescanning strategy, with rescans following the same direction as initial scans in a given layer, and with scanning rotated by 90 degrees between each layer. The cross-sectional dimensions of the rescan melt pools (blue) relative to the initial melt pools (orange) and the total thickness of each layer (t , approximately equal to the powder layer thickness) plays an important role in the spatial distribution of microstructural heterogeneity caused by rescanning. Referring to these dimensions, there are three expected scenarios:

- (i) If the combined height and depth of melt pool B, $(H+D)_B$, is greater or equal to height and depth of melt pool A, $(H+D)_A$ [i.e., $(H+D)_A - (H+D)_B \leq 0$], then $t_A = 0$ and the microstructure will be dominated by that of the rescanned melt pool B.
- (ii) If $0 < (H+D)_A - (H+D)_B < t$, the rescanned region will contain both initial and rescanning modified microstructure. The thickness of the initial scan region will be $t_A = (H+D)_A - (H+D)_B$ and the thickness of the rescanning modified microstructural region, $t_B = t - t_A$. Therefore, the microstructure of both the initial and rescanned tracks will be present.

(iii) If $(H+D)_A - (H+D)_B \geq t$, then $t_B = 0$ and the microstructure will be dominated by that of the initial melt pool A.

The dimensions of rescanned melt pools (B1, B2, B3, and B4) were measured and compared with initially scanned melt pools (A), as shown in Table 6. Based on the equations above, t_A and t_B were calculated and listed in Table 6. For all rescanned specimens, values of $(H+D)_B$ are smaller than $(H+D)_A$, indicating that none of these microstructures are dominated by rescanned melt pools alone [i.e. no cases of scenario (i)]. In specimen A+B2, t_A is larger than the powder layer thickness ($t = 30 \mu\text{m}$) and $t_B = 0$, as shown in Fig. 16 (c), and the rescanned tracks were covered by the next layers above [i.e. scenario (iii)]. All other rescanned specimens had values of t_A ranging from 0 to $30 \mu\text{m}$, indicating that both initial microstructure and modified microstructure exist in rescanning regions [i.e. scenario (ii)]. As shown in Fig. 16(b, d, and e), both orange and blue melt pools are visible. Among them, specimen A+B1 showed smallest proportion of blue rescanned melt pools in rescanning region with the smallest value of t_B .

Table 6 Measured depth + height (H+D) of initial and rescanned melt pool tracks in rescanned specimens. Values given are averages \pm one standard deviation.

	Specimen A+B1	Specimen A+B2	Specimen A+B3	Specimen A+B4
$(H+D)_A$ (μm)	50.67 ± 6.76	70.35 ± 9.35	62.67 ± 10.83	63.26 ± 9.74
$(H+D)_B$ (μm)	22.07 ± 2.62	16.47 ± 2.91	44.43 ± 4.98	45.80 ± 3.35
t_A (μm)	28.6	53.88	18.24	17.46
t_B (μm)	1.4	< 0	11.76	12.54

4. Conclusion

Laser rescanning during LPBF additive manufacture with 316LSS was experimentally and analytically investigated in order to locally control the sub-grain cell size while

maintaining high levels of densification with a commercially available 200 W single laser system. The main conclusions are:

- Within a range of P - v processing space from $50 \text{ W} < P < 200 \text{ W}$ and $50 \text{ mm/s} < v < 1600 \text{ mm/s}$, sub-grain cell sizes measured from single laser scans were statistically similar to those in parts from multilayer scans and rescanned regions. Therefore, single laser scan results can guide microstructural predictions for larger multilayer parts, which can save time and cost in fabricating and exploring cell size of complex-shape parts.
- Within a range of P/v values from 0.25 to 1 J/mm, sub-grain cell size can be correlated to P/v according to an empirical power law relationship based on predictions from the Wilson-Rosenthal equation. However, predicted melt pool dimensions for single laser scans were unreliable.
- Rescanning with different parameters locally refined cell size from $0.84 \mu\text{m}$ to $0.35 \mu\text{m}$ and increased local density by 0.21-0.42% from an initial value of 99.55%. The effect of cell size on hardness was negligible in this study, which may be due to the differences in dislocation density around refined sub-grain cells and the potential effects of dynamic recrystallization and recovery due to repeated heating cycles from scanning and rescanning.
- Parameters that resulted in a cell size of $0.34 \mu\text{m}$ and a low density of 91.2% under uniform processing with initial scanning only can be used as rescanning parameters to achieve a high density of 99.9% and the same refined cell size within the rescanned melt pools. Therefore, LPBF parameters that are

unsuitable for processing highly dense parts, can still be utilised as rescanning parameters for heterogeneous microstructural control.

- Rescanning produced microstructural heterogeneity in 316L SS with a spatial distribution that is determined by the relative size of initial and rescanned melt pools and the powder layer thickness.
 - (i) When rescan melt pools are largest, the refined microstructure from rescanning will dominate.
 - (ii) When the rescan melt pools are smaller than the initial scans, but larger than the powder layer height, both coarse and refined microstructures will result.
 - (iii) When the rescan melt pools are smaller than the initial scans and the powder layer height, the coarse microstructure from initial scanning will dominate.

Declaration of Competing Interest:

The authors report no declarations of interest.

Acknowledgments:

This work was supported by the faculty of Engineering and Physical Science at University of Southampton. The authors are also grateful for contributions of Dr. Dichu Xu (operation of Nanoindenter), Richard Dooler (operation of Concept Laser M2) and Geoff Howell (assistance with metallographic preparation).

Reference:

- ADDITIVE, C., 2019a. 316L Powder for Additive Manufacturing.
- Additive, G., 2019b. GE Additive 316L Datasheet.
- ASTM, 2015. ASTM E2546-15 Standard Practice for Instrumented Indentation Testing.
- ASTM, 2017. ASTM B962-17 Standard Test Methods for Density of Compacted or Sintered Powder Metallurgy (PM) Products Using Archimedes' Principle.
- Bertoli, U.S., MacDonald, B.E., Schoenung, J.M., 2019. Stability of cellular microstructure in laser powder bed fusion of 316L stainless steel. *Materials Science and Engineering: A* 739, 109-117.
- Casati, R., Lemke, J., Vedani, M., 2016. Microstructure and Fracture Behavior of 316L Austenitic Stainless Steel Produced by Selective Laser Melting. *Journal of Materials Science & Technology* 32, 738-744.
- Cherry, J.A., Davies, H.M., Mehmood, S., Lavery, N.P., Brown, S.G.R., Sienz, J., 2014. Investigation into the effect of process parameters on microstructural and physical properties of 316L stainless steel parts by selective laser melting. *The International Journal of Advanced Manufacturing Technology* 76, 869-879.
- Clymer, D.R., Cagan, J., Beuth, J., 2017. Power–Velocity Process Design Charts for Powder Bed Additive Manufacturing. *Journal of Mechanical Design* 139.
- Collins, P., Brice, D., Samimi, P., Ghamarian, I., Fraser, H., 2016. Microstructural control of additively manufactured metallic materials. *Annual Review of Materials Research* 46, 63-91.
- Demir, A.G., Previtali, B., 2017. Investigation of remelting and preheating in SLM of 18Ni300 maraging steel as corrective and preventive measures for porosity reduction. *The International Journal of Advanced Manufacturing Technology* 93, 2697-2709.
- Di, W., Yongqiang, Y., Xubin, S., Yonghua, C., 2011. Study on energy input and its influences on single-track, multi-track, and multi-layer in SLM. *The International Journal of Advanced Manufacturing Technology* 58, 1189-1199.
- Eagar, T., Tsai, N., 1983. Temperature fields produced by traveling distributed heat sources. *Welding journal* 62, 346-355.
- Griffiths, S., Rossell, M., Croteau, J., Vo, N., Dunand, D., Leinenbach, C., 2018. Effect of laser rescanning on the grain microstructure of a selective laser melted Al-Mg-Zr alloy. *Materials Characterization* 143, 34-42.
- Guo, Y., Jia, L., Kong, B., Wang, N., Zhang, H., 2018. Single track and single layer formation in selective laser melting of niobium solid solution alloy. *Chinese Journal of Aeronautics* 31, 860-866.
- Hao, L., Dadbakhsh, S., Seaman, O., Felstead, M., 2009. Selective laser melting of a stainless steel and hydroxyapatite composite for load-bearing implant development. *Journal of Materials Processing Technology* 209, 5793-5801.
- Hunziker, O., Dye, D., Reed, R., 2000. On the formation of a centreline grain boundary during fusion welding. *Acta Materialia* 48, 4191-4201.
- ISO, 2019. ISO 643:2017 Steels — Micrographic determination of the apparent grain size.
- Katayama, S., Matsunawa, A., 1984. Solidification microstructure of laser welded stainless steels, *International Congress on Applications of Lasers & Electro-Optics*. Laser Institute of America, pp. 60-67.
- Keller, C., Mokhtari, M., Vieille, B., Briatta, H., Bernard, P., 2020. Influence of a rescanning strategy with different laser powers on the microstructure and mechanical properties of Hastelloy X elaborated by powder bed fusion. *Materials Science and Engineering: A*, 140474.

King, A., Eckersley, R., 2019. Chapter 5. Inferential statistics II: parametric hypothesis testing, In: King, A., Eckersley, R. (Eds.), *Statistics for Biomedical Engineers and Scientists*, pp. 91-117.

King, W.E., Barth, H.D., Castillo, V.M., Gallegos, G.F., Gibbs, J.W., Hahn, D.E., Kamath, C., Rubenchik, A.M., 2014. Observation of keyhole-mode laser melting in laser powder-bed fusion additive manufacturing. *Journal of Materials Processing Technology* 214, 2915-2925.

Kistler, N.A., Nassar, A.R., Reutzel, E.W., Corbin, D.J., Beese, A.M., 2017. Effect of directed energy deposition processing parameters on laser deposited Inconel® 718: Microstructure, fusion zone morphology, and hardness. *Journal of Laser Applications* 29, 022005.

Li, Z., He, B., Guo, Q., 2020. Strengthening and hardening mechanisms of additively manufactured stainless steels: The role of cell sizes. *Scripta Materialia* 177, 17-21.

Matilainen, V., Piili, H., Salminen, A., Syvänen, T., Nyrhilä, O., 2014. Characterization of Process Efficiency Improvement in Laser Additive Manufacturing. *Physics Procedia* 56, 317-326.

Mills, K.C., 2002. Recommended values of thermophysical properties for selected commercial alloys. Woodhead Publishing.

Mukherjee, T., Wei, H., De, A., DebRoy, T., 2018. Heat and fluid flow in additive manufacturing—Part II: Powder bed fusion of stainless steel, and titanium, nickel and aluminum base alloys. *Computational Materials Science* 150, 369-380.

Niendorf, T., Leuders, S., Riemer, A., Brenne, F., Tröster, T., Richard, H.A., Schwarze, D., 2014. Functionally Graded Alloys Obtained by Additive Manufacturing. *Advanced Engineering Materials* 16, 857-861.

Promoppatum, P., Yao, S.-C., Pistorius, P.C., Rollett, A.D., 2017. A comprehensive comparison of the analytical and numerical prediction of the thermal history and solidification microstructure of Inconel 718 products made by laser powder-bed fusion. *Engineering* 3, 685-694.

Rosenthal, D., 1941. Mathematical Theory of Heat Distribution during Welding and Cutting. *Welding Journal* 20, 220-234.

Rubenchik, A., Wu, S., Mitchell, S., Golosker, I., LeBlanc, M., Peterson, N., 2015. Direct measurements of temperature-dependent laser absorptivity of metal powders. *Applied optics* 54, 7230-7233.

Sabzi, H.E., Aboulkhair, N.T., Liang, X., Li, X.-H., Simonelli, M., Fu, H., Rivera-Díaz-del-Castillo, P.E., 2020. Grain refinement in laser powder bed fusion: The influence of dynamic recrystallization and recovery. *Materials & Design* 196, 109181.

Saunders, M., 2017. X marks the spot - find ideal process parameters for your metal AM parts.

Scipioni Bertoli, U., MacDonald, B.E., Schoenung, J.M., 2019. Stability of cellular microstructure in laser powder bed fusion of 316L stainless steel. *Materials Science and Engineering: A* 739, 109-117.

Shiomi, M., Osakada, K., Nakamura, K., Yamashita, T., Abe, F., 2004. Residual stress within metallic model made by selective laser melting process. *CIRP Annals* 53, 195-198.

Tian, Y., Gora, W.S., Cabo, A.P., Parimi, L.L., Hand, D.P., Tammis-Williams, S., Prangnell, P.B., 2018. Material interactions in laser polishing powder bed additive manufactured Ti6Al4V components. *Additive Manufacturing* 20, 11-22.

Trapp, J., Rubenchik, A.M., Guss, G., Matthews, M.J., 2017. In situ absorptivity measurements of metallic powders during laser powder-bed fusion additive manufacturing. *Applied Materials Today*, 9, 341-349.

Wang, X., Muñiz-Lerma, J.A., Sánchez-Mata, O., Attarian Shandiz, M., Brochu, M., 2018. Microstructure and mechanical properties of stainless steel 316L vertical struts manufactured by laser powder bed fusion process. *Materials Science and Engineering: A* 736, 27-40.

Wei, K., Lv, M., Zeng, X., Xiao, Z., Huang, G., Liu, M., Deng, J., 2019. Effect of laser remelting on deposition quality, residual stress, microstructure, and mechanical property of selective laser melting processed Ti-5Al-2.5 Sn alloy. *Materials Characterization* 150, 67-77.

Xiao, Z., Chen, C., Hu, Z., Zhu, H., Zeng, X., 2020. Effect of rescanning cycles on the characteristics of selective laser melting of Ti6Al4V. *Optics & Laser Technology* 122, 105890.

Yasa, E., Kruth, J.-P., Deckers, J., 2011. Manufacturing by combining selective laser melting and selective laser erosion/laser re-melting. *CIRP annals* 60, 263-266.

Yasa, E., Kruth, J.P., 2011. Microstructural investigation of Selective Laser Melting 316L stainless steel parts exposed to laser re-melting. *Procedia Engineering* 19, 389-395.

Ye, J., Rubenchik, A.M., Crumb, M.F., Guss, G., Matthews, M.J., 2018. Laser absorption and scaling behavior in powder bed fusion additive manufacturing of metals, *CLEO: Science and Innovations*. Optical Society of America, p. JW2A. 117.

Yu, W., Sing, S.L., Chua, C.K., Tian, X., 2019. Influence of re-melting on surface roughness and porosity of AlSi10Mg parts fabricated by selective laser melting. *Journal of Alloys and Compounds* 792, 574-581.

Yusuf, S., Chen, Y., Boardman, R., Yang, S., Gao, N., 2017. Investigation on Porosity and Microhardness of 316L Stainless Steel Fabricated by Selective Laser Melting. *Metals* 7.

Zhang, B., Li, Y., Bai, Q., 2017. Defect Formation Mechanisms in Selective Laser Melting: A Review. *Chinese Journal of Mechanical Engineering* 30, 515-527.